The Astrophysical Journal, 909:186 (17pp), 2021 March 10 https://doi.org/10.3847/1538-4357/abe122

A Broadband X-Ray View of the Precessing Accretion Disk and Pre-eclipse Dip in the Pulsar Her X-1 with NuSTAR and XMM-Newton

McKinley C. Brumback[1,2], Ryan C. Hickox[1], Felix S. Fürst[3], Katja Pottschmidt[4,5], John A. Tomsick[6], Jörn Wilms[7], Rüdiger Staubert[8], and Saeqa Vrtilek[9]
[1] Department of Physics & Astronomy, Dartmouth College, 6127 Wilder Laboratory, Hanover, NH 03755, USA
[2] Cahill Center for Astronomy and Astrophysics, California Institute of Technology, 1216 E California Blvd, Pasadena, CA 91125, USA
[3] European Space Astronomy Centre (ESA/ESAC), Operations Department, Villanueva de la Cañada, Madrid, Spain
[4] CRESST, Department of Physics and Center for Space Science and Technology, UMBC, Baltimore, MD 210250, USA
[5] NASA Goddard Space Flight Center, Code 661, Greenbelt, MD 20771, USA
[6] Space Sciences Laboratory, University of California, Berkeley, 7 Gauss Way, Berkeley, CA 94720, USA
[7] Dr. Karl Remeis-Sternwarte and Erlangen Centre for Astroparticle Physics, Sternwartstrasse 7, D-96049 Bamberg, Germany
[8] Institut für Astronomie und Astrophysik, Universität Tübingen, Sand 1, D-72076 Tübingen, Germany
[9] Harvard-Smithsonian Center for Astrophysics, 60 Garden Street, Cambridge, MA 02138, USA
Received 2020 August 6; revised 2021 January 26; accepted 2021 January 27; published 2021 March 17

Abstract

We present a broadband X-ray timing study of the variations in pulse behavior with the superorbital cycle in the low-mass X-ray binary Her X-1. This source shows a 35 day superorbital modulation in X-ray flux that is likely caused by occultation by a warped, precessing accretion disk. Our data set consists of four joint XMM-Newton and NuSTAR observations of Her X-1 which sample a complete superorbital cycle. We focus our analysis on the first and fourth observations, which occur during the bright "main-on" phase, because these observations have strongly detected pulsations. We added an archival XMM-Newton observation during the "short-on" phase of the superorbital cycle because our observations at that phase are lower in signal to noise. We find that the energy-resolved pulse profiles show the same shape at similar superorbital phases, and the profiles are consistent with expectations from a precessing disk. We demonstrate that a simple precessing accretion disk model is sufficient to reproduce the observed pulse profiles. The results of this model suggest that the similarities in the observed pulse profiles are due to reprocessing by a precessing disk that has returned to its original precession phase. We determine that the broadband spectrum is well fit by an absorbed power law with a soft blackbody component and show that the spectral continuum also exhibits a dependence on the superorbital cycle. We also present a brief analysis of the energy-resolved light curves of a pre-eclipse dip, which shows soft X-ray absorption and hard X-ray variability during the dip.

Unified Astronomy Thesaurus concepts: Pulsars (1306); Low-mass x-ray binary stars (939)

1. Introduction

Magnetically dominated accretion occurs regularly in the environments surrounding neutron stars that accrete from a stellar companion via mass transfer mechanisms such as stellar outflows and Roche lobe overflow (e.g., Nagase 2001). Near the pulsar's magnetosphere, magnetic pressure from the strong magnetic field overwhelms the ram pressure from the accretion disk, which causes the hot, ionized gas to accrete along the dipolar field lines. The structure of the accretion disk and magnetized accretion flow are thought to be complex in nature (e.g., Ogilvie & Dubus 2001; Romanova et al. 2002, 2003, 2004); however, observational constraints on magnetically dominated accretion structures are limited.

The luminous X-ray pulsars LMC X-4, SMC X-1, and Her X-1 show superorbital periods, which are variations on timescales longer than the orbital period. These superorbital periods are attributed to warped disks, where radiation pressure drives a tilt in the accretion disk (e.g., Pringle 1996; Ogilvie & Dubus 2001). As the disk precesses, the warped edge temporarily occults the pulsar and causes changes in luminosity. The geometry of the accretion disk and the neutron star in these warped disk systems creates some of the best observational laboratories for studying magnetized accretion flow onto compact objects because emission from the accretion and reprocessed emission from the accretion disk can both be detected (Hickox et al. 2004). Brumback et al. (2020; hereafter B20) used pulse phase-resolved spectroscopy and tomography to model the warped inner accretion disk structure around the bright X-ray pulsars LMC X-4 and SMC X-1. This analysis assumed that the superorbital period, which is present on timescales of 30–60 days in these sources, is caused by the precession of a warped inner accretion disk seen approximately edge on (e.g., Gerend & Boynton 1976; Heemskerk & van Paradijs 1989; Wojdowski et al. 1998). In sources with this accretion disk geometry, the rotating, high-energy beam from the neutron star irradiates the inner accretion disk. The disk reprocesses the beam's radiation and releases softer X-rays, which differ in pulsation shape and phase from the hard pulses (Shulman et al. 1975; Neilsen et al. 2004; Zane et al. 2004; Hickox & Vrtilek 2005). B20 used the simple geometric warped disk model created by Hickox & Vrtilek (2005) to model observed changes in the hard and soft pulse profile shapes as a function of the superorbital phase in LMC X-4 and SMC X-4 with broadband X-ray coverage.

In this work, we will follow the method of B20 and provide observational constraints on the geometry of the warped inner accretion disk in Her X-1, a prototype X-ray pulsar (Tananbaum et al. 1972), making use of full hard X-ray coverage from the Nuclear Spectroscopic Telescope Array (NuSTAR). Her X-1 is a low-mass X-ray binary consisting of a 1.5 $M_{\odot}$ neutron star orbiting HZ Herculis, an approximately 2.2

$M_\odot$ A/F-type star (Crampton & Hutchings 1974; Deeter et al. 1981; Reynolds et al. 1997). The binary orbit is 1.7 days and is nearly circular (Staubert et al. 2009). The orbital plane is highly inclined ($i = 85°$–$88°$), resulting in regular eclipses of the neutron star. The distance to the binary is 6.6 kpc (Reynolds et al. 1997). Her X-1 is a cyclotron line source (Truemper et al. 1978), with a broad absorption feature caused by cyclotron resonance scattering being visible in the hard X-ray spectrum. The energy at which this feature occurs is caused by the strength of the pulsar's magnetic field, and thus, the feature allows astronomers to directly measure the field strength. The central energy of this cyclotron resonance scattering feature (CRSF) has been found to correlate strongly with the source flux (Staubert et al. 2007, 2016, 2017). In addition, the energy shows an interesting evolution with time: after a fairly constant value around 37 keV for about a decade after the discovery, a strong turn-up occurred to beyond 40 keV (Gruber et al. 2001), followed by a nearly 20 yr decline until ∼2012, after which the line energy is again constant around 37 keV (Staubert et al. 2016, 2020; Bala et al. 2020). This value suggests that the magnetic field in Her X-1 is approximately 3.2×10^{12} G (Staubert et al. 2020). Tananbaum et al. (1972) discovered 1.24 s X-ray pulsations from the neutron star and a longer, approximately 35 day modulation in X-ray luminosity.

This 34.85 day superorbital period in Her X-1 is likely caused by a warped, precessing inner accretion disk (Giacconi et al. 1973; Ramsay et al. 2002; Zane et al. 2004). The superorbital period consists of a bright "main-on" period lasting approximately 11 days and a shorter, fainter "short-on" period lasting approximately 8 days separated by 8 day off states (Tananbaum et al. 1972; Giacconi et al. 1973). During the bright main-on state, Her X-1 reaches characteristic X-ray luminosities of approximately 10^{37} erg s^{-1}. During the 35 day cycle, the neutron star eclipses every 1.7 days, and there are additional pre-eclipse dips seen every 1.62 days (Jones & Forman 1976). These pre-eclipse dips are likely caused by obscuration of the pulsar by material at the interaction point between the accretion stream and the disk (e.g., Still et al. 2001). Another feature of the superorbital behavior in Her X-1 are the anomalous low states, which are defined by a significant decrease in X-ray flux and pulsation strength without a significant change in the optical and UV flux (e.g., Vrtilek & Cheng 1996; Coburn et al. 2000; Staubert et al. 2017). These states can last for several months and are likely caused by a change in the scale height of the accretion disk, which obscures the central accretor, or a change in disk inclination (e.g., Parmar et al. 1985).

In this work, we present joint XMM-Newton and NuSTAR observations of Her X-1 that sample a single superorbital cycle, allowing us to monitor and model the precession of the accretion disk. Although the source is well studied, previous Her X-1 observations lack the combination of energy coverage, timing resolution, and sampling of different phases within a single superorbital cycle needed to fully constrain the pulsar beam and disk geometry over the precession cycle of the disk. Ramsay et al. (2002) and Zane et al. (2004) used XMM-Newton to observe the precession of the inner accretion disk, but their analysis lacked NuSTAR high-energy coverage. Fürst et al. (2013) illustrated the importance of high-energy pulse profiles in Her X-1 by showing the dramatic changes in pulse shape and phase that occur across the NuSTAR energy band. However, the Fürst et al. (2013) observations took place during one superorbital phase so they could not demonstrate changes in pulse profile at different superorbital phases. McCray et al. (1982) and Vrtilek & Halpern (1985) had soft X-ray coverage of a complete 35 day cycle of Her X-1 with Einstein's MPC. However, Einstein's energy range of 1–20 keV does not fully constrain changes in the soft pulsations, which Hickox et al. (2004) found peak below 1 keV. Staubert et al. (2013) demonstrated the variability of the pulse profiles of Her X-1 as a function of the superorbital phase, their observations do not have the soft X-ray coverage necessary to capture reprocessed emission (less than 1 keV) from the accretion disk.

In this paper, we use both NuSTAR and XMM-Newton in order to conduct a broadband study of the pulse profiles and spectral shapes of Her X-1 during two consecutive main-on states of the superorbital cycle, allowing us to test the periodic dependence of these features. We also supplement our observations with archival observations that allow us to study the short-on state of the superorbital cycle.

In Section 2, we describe the previously unpublished joint XMM-Newton and NuSTAR observations of Her X-1, as well as some archival data used in this analysis. In Section 3, we describe the procedure used to extract pulse profiles and perform phase-averaged and phase-resolved spectroscopy, and we present the results in Section 4. In Section 5, we model the observed pulse profiles and simulate the inner disk geometry. We briefly examine the energy-resolved light curves of a pre-eclipse dip in one of our observations in Section 6. In Section 7, we discuss the implication of our results.

2. Observations

The data used in this analysis are a set of four joint NuSTAR (Harrison et al. 2013) and XMM-Newton observations of Her X-1 that took place between 2019 February 9 and March 14. Following the convention used in B20, we refer to these observations as Observations H1, H2, H3, and H4. Table 1 shows the date of observation, the observation ID number, superorbital phase, and exposure time for each observation. Figure 1 shows the one-day-averaged MAXI light curve, folded on the 35 day superorbital period, for Her X-1 with the observations plotted as red vertical lines.

We reduced these data using HEASoft version 6.26.1 with NuSTAR CALDB v20191219 and XMMSAS version 18.0.0. For the NuSTAR observations, we selected a circular source region of radius 110″ with DS9 (Joye & Mandel 2003). We used a circular region of the same size away from the source as the background region. The background counts make up approximately 0.3% of the total counts. For the XMM-Newton observations, we used the EPIC-pn instrument in Timing Mode exclusively to obtain the maximum possible timing resolution and to minimize the effects of pileup, and selected only single and double events from the EPIC-pn data. We used the XMMSAS tool epatplot to evaluate the observations for pileup by comparing the model of expected single and double events to data. In the observations that took place during Her X-1's bright main-on phase (obsIDs 0830530101 and 0830530401), we found differences in the models indicative of pileup. We excised the brightest central pixels and examined the models again until we found good agreement. Ultimately, we found it was only necessary to exclude the central pixel to reduce pileup.

We performed a barycentric correction to Observations H1–H4 using the NuSTARDAS tool barycorr and the XMMSAS

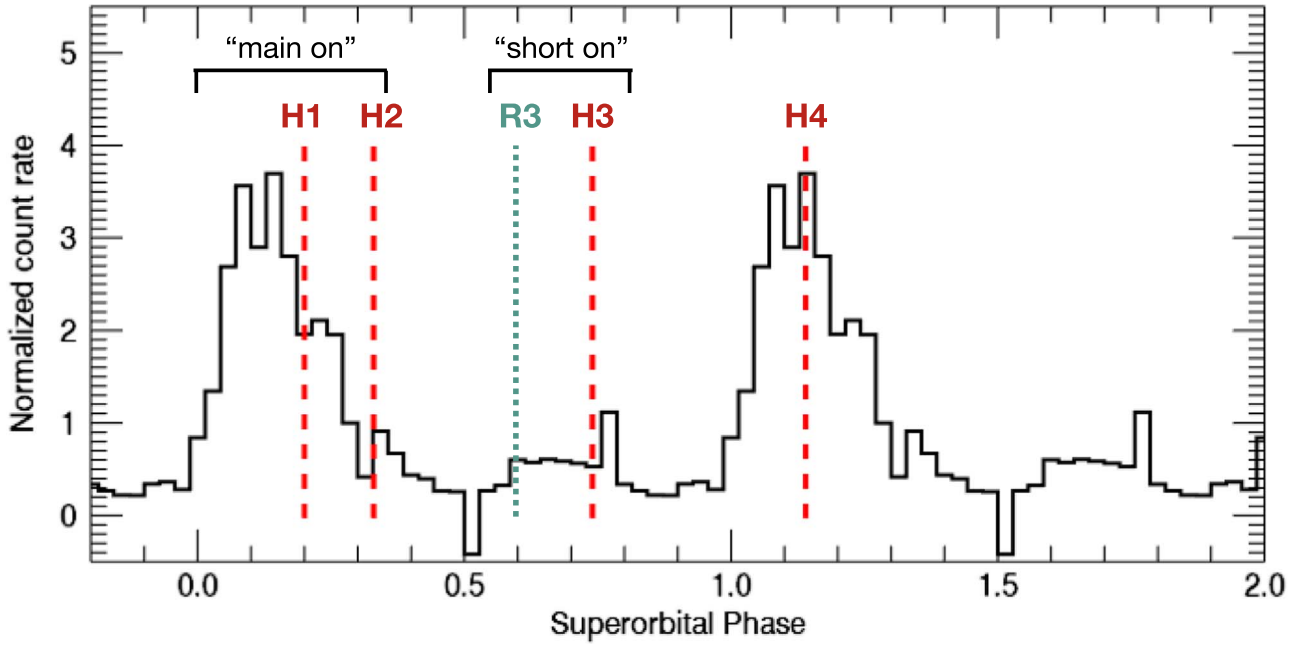

Figure 1. The one-day-averaged 2–20 keV MAXI (Matsuoka et al. 2009) light curve of Her X-1, which we folded on the 35 day superorbital cycle and plotted twice for clarity. We show the times of the joint XMM-Newton and NuSTAR observations used in this analysis as red vertical, dashed lines. We label Observations H1 through H4 to show their place in this series. The teal vertical dotted line shows the superorbital phase of the archival XMM-Newton observation 0111061201; this is the third observation in a series of observations first analyzed by Ramsay et al. (2002), which we refer to as Observation R3. The main-on and short-on time periods of the superorbital cycle are marked with brackets.

Table 1
Description of Her X-1 Observations[a]

Name	Date	Mid-exposure Time (MJD)	ϕ_{SO}	Observation ID	Observatory	Telescope Mode	Exposure (ks)
H1	09 Feb 2019	58523.619	0.20	30402034002	NuSTAR	⋯	18.2
H1	09 Feb 2019	58523.669	0.20	0830530101	XMM-Newton	Fast Timing Mode	21.9
H2	13 Feb 2019	58528.147	0.33	30402034004	NuSTAR	⋯	22.0
H2	13 Nov 2019	58528.131	0.33	0830530201	XMM-Newton	Fast Timing Mode	27.2
R3[b]	16 Mar 2001	51984.992	0.60	0111061201	XMM-Newton	Fast Timing Mode	11
H3	28 Feb 2019	58542.515	0.74	30402034006	NuSTAR	⋯	23.0
H3	28 Feb 2019	58542.534	0.74	0830530301	XMM-Newton	Fast Timing Mode	32.6
H4	14 Mar 2019	58556.515	1.14	30402034008	NuSTAR	⋯	16.7
H4	14 Mar 2019	58556.523	1.14	0830530401	XMM-Newton	Fast Timing Mode	29.1

Notes.
[a] These observations span two consecutive superorbital cycles. The turn on for the first cycle was 58516.6 MJD, and the turn on for the second cycle was 58551.5 MJD.
[b] This is the third observation in an archival data set of Her X-1 first presented in Ramsay et al. (2002) and later used in Zane et al. (2004) and Jimenez-Garate et al. (2002). In this work, we use Observation R3 as an alternative to the weak pulsations in Observation H3.

tool barycen. We accounted for the effect of the neutron star's orbit by correcting the photon arrival times using the Her X-1 orbital ephemeris described in Staubert et al. (2009).

We show the NuSTAR 3–79 keV and XMM-Newton 0.2–15 keV light curves for the Her X-1 observations in Figure 2. The XMM-Newton count rates have been arbitrarily offset from the NuSTAR count rates in Observations H2, H3, and H4 for clarity. Observation H4 captured a pre-eclipse dip with both telescopes. We also show the pulsed fractions for the NuSTAR 3–79 keV data and the XMM-Newton 0.3–0.7 keV data overplotted with the light curves. Plotting the hard and soft pulsed fractions allowed us to determine which parts of the data set were suitable for our analysis, which required both hard and soft pulsations (see Section 5). For this reason, we did not include Observation H2 (where pulsations were not detected in XMM-Newton or NuSTAR), Observation H3 (where XMM-Newton pulsations were not detected), or data after the onset of the dip in H4 (where the soft pulses dramatically weaken).

Because we were unable to extract both hard and soft pulse profiles from Observations H2 and H3, we turned to archival data of Her X-1 to increase our coverage of the 35 day superorbital cycle. As mentioned in the introduction, many previous works have presented changes in the pulse profile shape across the superorbital cycle. We focused on the XMM-Newton data archive because the 0.2–12 keV energy range would allow us to directly compare the soft data to our observations while offering some overlap with our NuSTAR data. For the sake of brevity, we selected a single archival XMM-Newton observation of Her X-1. ObsID 0111061201 took place on 2001 March 16 as part of a series of XMM-Newton observations of Her X-1 and was first presented in Ramsay et al. (2002). Because this observation is the third in its

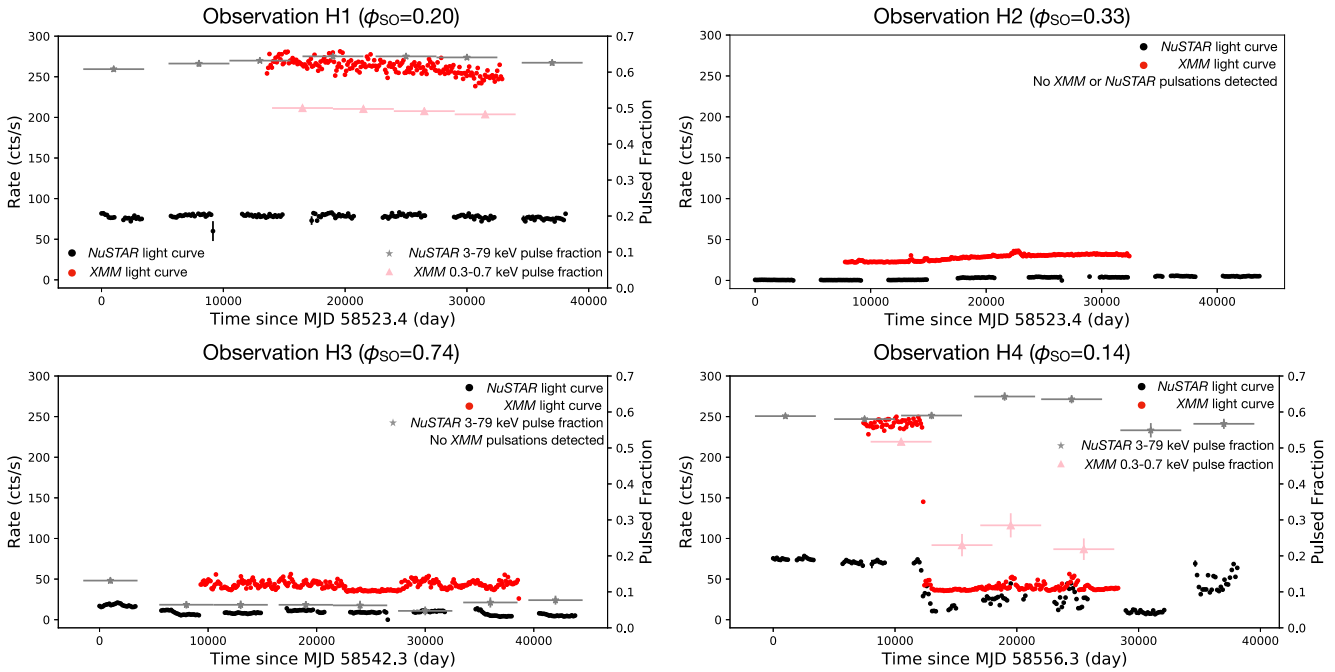

Figure 2. NuSTAR 3–79 keV (black) and XMM-Newton 0.2–12 keV (red) light curves of the four joint Her X-1 observations. We also show the pulsed fractions, discussed in Section 3, for the 3–79 keV NuSTAR data (gray stars) and 0.3–0.7 keV XMM-Newton data (pink triangles) where pulsations are detected. We offset the XMM-Newton light curves by a value of 20 in Observations H2 and H3 and 30 in Observation H4 for clarity. A pre-eclipse dip is visible in both the NuSTAR and XMM-Newton light curves of Observation H4. For this analysis, we only used data where pulsations were strongly detected in both XMM-Newton and NuSTAR. For clarity, we have filtered the light curves of the bright Observations H1 and H4 in order to remove bins with low exposure fraction caused by XMM-Newton's Counting Mode.

original series, we refer to it as Observation R3 in this work. Observation R3 took place at superorbital phase 0.60. We reduced these data following the analysis steps described in Ramsay et al. (2002), which are broadly consistent with the reduction process described in this work. However, we added the correction described in Ramsay et al. (2002) to FTCOARSE, which had erroneously incremented by 1 s during this observation. As in Ramsay et al. (2002), we only examine the EPIC-pn data to minimize pileup. We used the XMMSAS tool barycen to apply a barycentric correction to this data set. However, we did not use the Still et al. (2001) orbital ephemeris for Her X-1, which was used by Ramsay et al. (2002), and instead chose to correct the photon arrival times with the more recently updated Staubert et al. (2009) ephemeris.

Table 2
Best-fit Spin Periods for Her X-1 Observations

Observation	Spin Period (s)[a]
H1	1.237721(6)
H2	N/A
H3	1.2377(4)
R3	1.2379(2)
H4	1.237721(8)

Note.
[a] For Observations H1–H4, we used NuSTAR 3–79 keV data to determine the pulse period. For Observation R3, we used XMM-Newton EPIC-pn 0.2–12 keV data.

3. Data Analysis

3.1. Timing Analysis

We used HENDRICS's Z_4^2 statistics search, which is functionally similar to epoch folding, to determine the spin period and spin period derivative of each observation (Buccheri et al. 1983; Bachetti 2015). For all observations used in this work, we found that the spin period derivative was consistent with zero. We estimated the uncertainty in the spin period by creating pulse profiles from the beginning and end of each observation and calculating $\delta_{\rm frequency} = \delta_{\rm phase}/\delta_{\rm time}$. While we were able to precisely measure the spin period in Observations H1 and H4 due to their length and good signal-to-noise ratio, the fainter observations (which do not show pulsations across the entire observations) had higher uncertainties, as can be seen in Table 2. We do not list any period for Observation H2 because we were unable to detect pulsations during this observation. All errors are 90% confidence unless otherwise specified.

For the archival data set, Observation R3, our use of a different orbital ephemeris necessitated redoing the pulsation search, which we did using the method described above. We detected pulsations with a spin period of 1.2379 ± 0.0001 s, which is slightly larger than the best period found by Ramsay et al. (2002). This difference is most likely caused by the use of a different orbital ephemeris. To check for consistency with Ramsay et al. (2002), we extracted energy-resolved pulse profiles in a soft band of 0.3–0.7 keV and a hard band of 8–12 keV. We found good agreement between our energy-resolved pulse profiles and those presented in Figure 2 of Ramsay et al. (2002).

We filtered the Observations H1 and H4 data sets by energy, selecting the 8–60 keV energy range from the NuSTAR data and the 0.3–0.7 keV energy range from the XMM-Newton data. We selected these energy ranges specifically for two

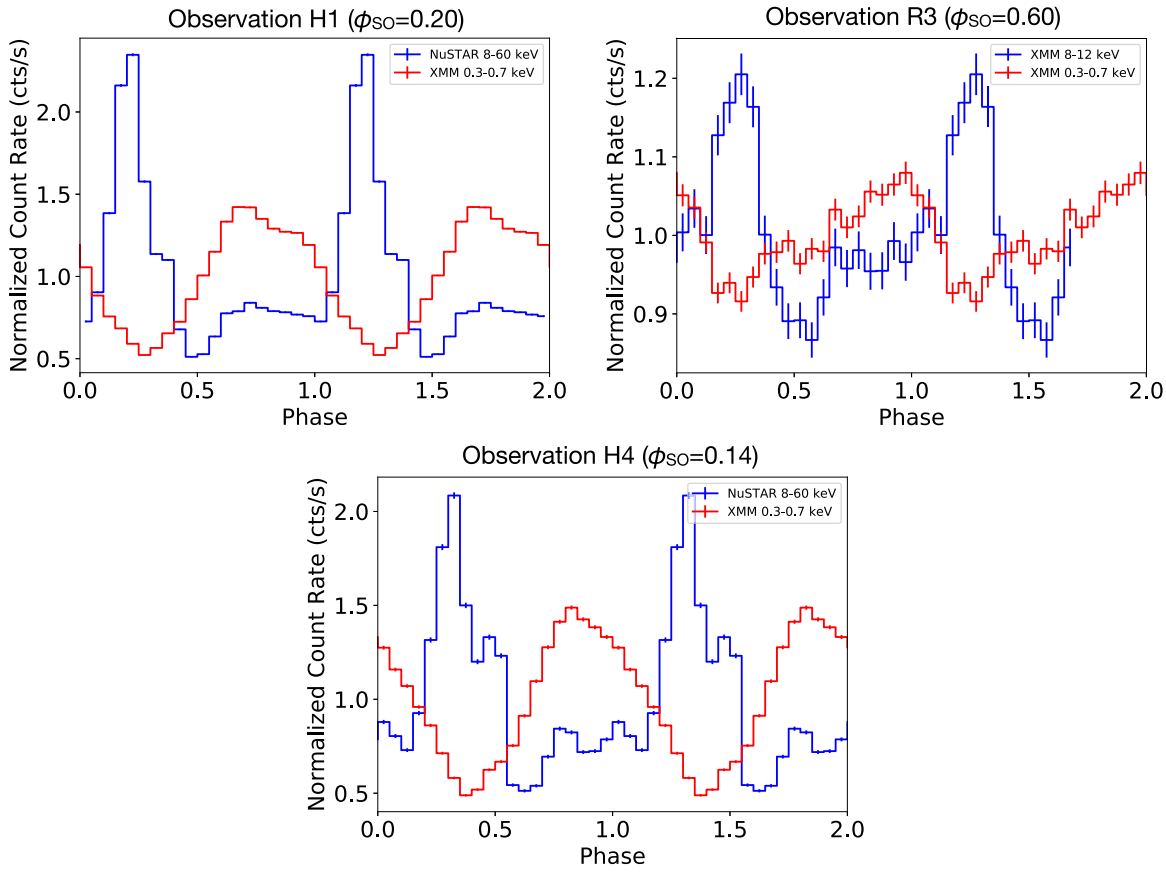

Figure 3. Joint pulse profiles for the Her X-1 observations H1, R3, and H4. The same relative phase shift between the NuSTAR 8–60 keV pulse profile (blue) and the XMM-Newton 0.3–0.7 keV pulse profile (red) is visible in Observations H1 and H4, which we expected because these observations occur at similar superorbital phases. However, the soft pulse profile shown in Observation R3 shows a change in shape and relative phase because of its different superorbital phases. To highlight these relative phase shifts, we shifted the pulse profiles of R3 and H4 so that the hard peaks were aligned with those of Observation H1. The slight difference between superorbital phase 0.20 (Observation H1) and 0.14 (Observation H4) can be seen in the subtle differences in the shape of the NuSTAR pulse profile.

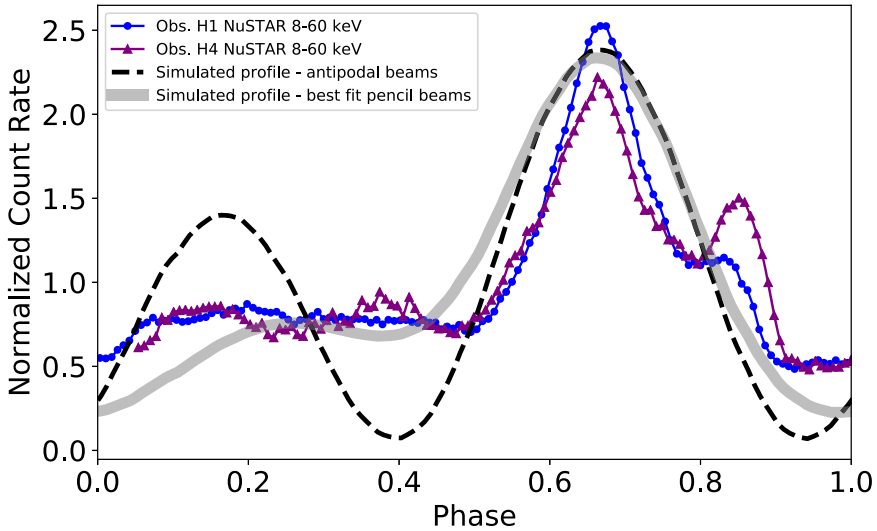

Figure 4. Pulse profiles in the hard NuSTAR band for Observation H1 (blue circles) and Observation H4 (purple triangles) binned with 128 bins per phase. Fine structure in the hard pulse profiles is visible, including two bumps within the interpulse of Observation H4 and a notch in the main pulse of both observations. The differences in fine structure between Observations H1 and H4 originate from the small difference in superorbital phase between these observations, which emphasizes that the pulse profiles are excellent trackers of the superorbital phase (e.g., Fürst et al. 2013; Staubert et al. 2013). We also show the simulated pulse profiles from an antipodal pencil-beam configuration (black dashed line) and our best-fit non-antipodal pencil beam (gray line) from our warped disk model (see Section 5). Both of these simulated pulse profiles were binned with 128 bins per phase and smoothed with a Savitzky–Golay filter. Our warped disk model is not capable of reproducing fine structure in the pulse profiles, and we therefore fit the coarser structure. We can also see that an antipodal beam geometry is insufficient to describe the hard pulse shape in Her X-1 with our model.

reasons. The first is to separate soft, reprocessed emission (less than 1 keV) from the accretion disk and hard emission from the pulsar beam. The second was that an analysis of the energy-resolved pulse profiles indicated changes in the soft pulse profile beginning at approximately 0.8 keV. We show the energy-resolved pulse profiles and discuss those results in more detail in the Appendix.

We then used the epoch-folding tool fold_events from the Stingray (Huppenkothen et al. 2019) software to create energy-resolved pulse profiles (see Figure 3). The pulse profiles in Figure 3 contain 20 bins per pulse phase. We selected this binning based on the resolution of our simulated pulse profiles, which are not capable of reproducing fine structure within the pulse profile (see Figure 4 and discussion in Sections 4 and 5). When making the pulse profiles, we used the start time of each observation as phase zero for that pulse profile because we are interested in the relative change in phase between hard and soft profiles rather than the phase difference between observations. However, to highlight these relative phase shifts, we shifted the pulse profiles of R3 and H4 so that the hard peaks were aligned with those of Observation H1.

Using the above method, we were also able to create a pulse profile from the NuSTAR data of Observation H3. While we could not use this observation in our modeling analysis due to the lack of detected XMM-Newton pulsations, we show the NuSTAR pulse profile in the Appendix for completeness.

For data where pulsations were detected, we calculated the pulsed fractions by first dividing the XMM-Newton and NuSTAR data into 5 ks time intervals. For each of these time intervals, we calculated the pulsed fractions that we showed in Figure 2 as $PF = (P_{\max} - P_{\min})/(P_{\max} + P_{\min})$, where $P_{\max}$ is the maximum of the pulse profile and $P_{\min}$ is the minimum of the profile. The errors were calculated from a distribution of 100 pulse profiles made with randomly selected periods between 0.5–1 and 1.25–2 s (that is, close to but not precisely the actual pulse period).

3.2. Phase-averaged Spectroscopy

To create joint spectra, we extracted NuSTAR and XMM-Newton source and background spectra from the regions described in Section 2 using NuSTARDAS and XMMSAS, respectively. However, we did not extract background spectra from the XMM-Newton data because the high source flux dominated the EPIC-pn CCD in Timing Mode, leaving no source-free region for background calculation (e.g., Ng et al. 2010). We grouped the NuSTAR spectra into bins with a signal-to-noise ratio of 10 and the XMM-Newton spectra with 100 counts per bin. In order to fit the spectra over our desired energy range of 0.3–60 keV, for consistency with our timing analysis, we were required to use XMM-Newton data outside of the nominal calibration range of 0.7–12 keV for EPIC-pn in Timing Mode. We do not believe this affected the quality of our spectral fits because the features at low energies (the blackbody component and 1 keV bump feature; see below) are strongly preferred by the data and have been seen before in this source (e.g., Jimenez-Garate et al. 2002; Hickox et al. 2004).

We fitted the phase-averaged spectrum over the 0.3–60 keV energy range using Xspec version 12.10.1 (Arnaud 1996). We found that the double power-law parameters were degenerate with the absorption models used to describe the CRSF when using the Negative and Positive EXponential (NPEX; e.g., Mihara et al. 1998) to describe the continuum (as was done B20). Therefore, we used a continuum model of a power law with a high-energy cutoff (powerlaw*highecut) that did not show degeneracy. This continuum model creates a discontinuity at the cutoff energy that we corrected for by adding a Gaussian absorption feature with its energy tied to the cutoff energy and a free width and depth (e.g., Coburn et al. 2002 and references therein).

Following the spectral model of B20, we also included an absorbing column (tbnew), a blackbody with $kT \sim 0.1$ keV, and several Gaussian emission lines corresponding to Fe Kα (6.4 keV) and a $\approx$1 keV "bump." This continuum bump at 1 keV has been previously observed in Her X-1 with XMM-Newton's RGS instrument (Jimenez-Garate et al. 2002) and with Suzaku (Fürst et al. 2013). Both Jimenez-Garate et al. (2002) and Fürst et al. (2013) suggest that this feature is an unresolved complex of lines from Ne and Fe. The XMM-Newton EPIC-pn camera does not have the spectral resolution to resolve the complex structure of these features and, therefore, we allowed for a single Gaussian emission line at 0.9 keV that encompassed the "bump" and described the shape of the spectrum phenomenologically. We allowed the Fe Kα line to contain both a broad ($\sigma = 0.5$ keV) and a narrow ($\sigma = 0.1$ keV) component. The Fe emission at 6.4 keV has been shown in previous works to be associated with near-neutral iron within the inner accretion disk and accretion column (e.g., Pravdo et al. 1978; Leahy 2000).

We fixed the absorbing column density to 1.5×10^{20} cm^{-2}, which we calculated using the HI4PI Map (HI4PI Collaboration et al. 2016) and the HEASARC $N_{\rm H}$ calculator. We set the abundances to those described in Wilms et al. (2000) and the cross sections to those from Verner et al. (1996).

Unlike LMC X-4 and SMC X-1, which were modeled in B20, Her X-1 is a cyclotron line source. To model the CRSF, we tested two possible models: the Gaussian absorption model gabs and the cyclotron absorption model cyclabs (e.g., Mihara et al. 1990). While we found that both models were capable of fitting the CRSF with a similar reduced χ^2, the cyclabs model proved degenerate with the continuum model, resulting in unreasonable values for the CRSF energy and the power-law folding energy. Additionally, the gabs model is used by Staubert et al. (2020) in their long-term monitoring of Her X-1's CRSF, and using gabs in our spectral models provides results that are consistent with their analysis. For these reasons, we used the gabs model in both observations.

We show the phase-averaged spectra and the residuals to our model fit for Observations H1, H2, H3, and H4 in Figure 5. In Figure 5, we show the joint XMM-Newton and NuSTAR spectrum in the first panel, the ratio of data to model for our best-fit spectral model in the middle panel, and the ratio of data to model for our best-fit model without the absorption feature representing the CRSF in the bottom panel. The bottom panels of Figure 5 demonstrate that the presence of a CRSF in the model is strongly preferred by the data for each observation. We note that Observations H2 and H3, which were fainter than the other two observations, have reduced signal at high energies, which made the CRSF absorption model less well constrained compared to Observations H1 and H4. In order to fit our spectral model while including the CRSF, we fixed the

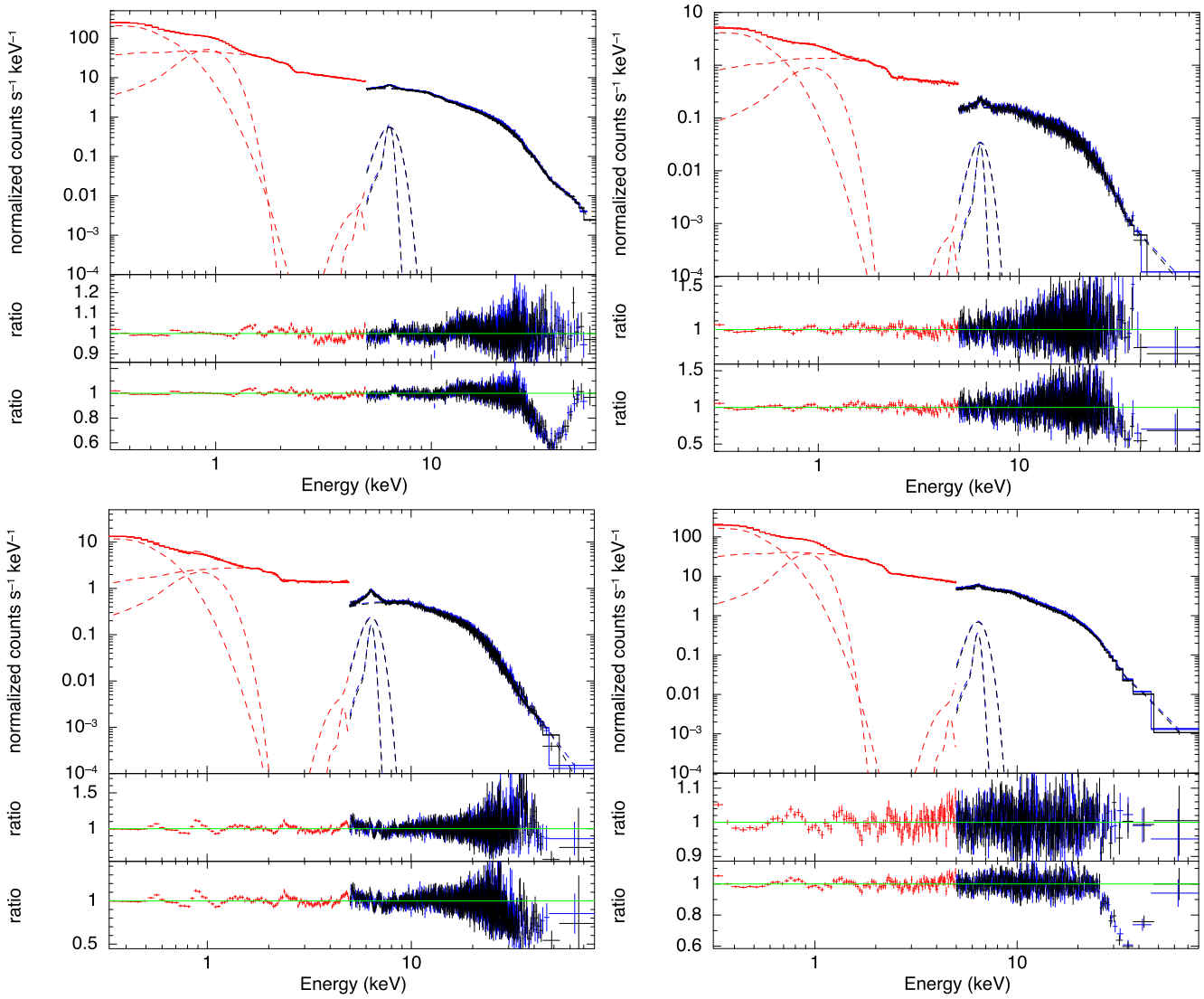

Figure 5. Joint XMM-Newton (red) and NuSTAR (FPMA—blue, FPMB—black) spectra for the Her X-1 observations H1 ($\phi_{SO} = 0.22$, top-left panel), H2 ($\phi_{SO} = 0.33$, top-right panel), H3 ($\phi_{SO} = 0.74$, bottom-left panel), and H4 ($\phi_{SO} = 0.16$, bottom-right panel). The XMM-Newton spectrum is modeled from 0.3–5 keV, while the NuSTAR spectra are modeled from 5–60 keV. For each spectrum, the top panel shows the spectrum and model components, the middle panel shows the ratio of data to model for the best-fit model, and the bottom panel shows the ratio of data to model with the CRSF feature removed. Table 3 contains the spectral parameters.

values for line energy, width, and strength in Observations H2 and H3 to the average of the CRSF model parameters in Observations H1 and H4. Table 3 contains the spectral parameters.

We also calculated the flux of the entire modeled spectrum (0.3–60 keV) and the high-energy band (8–60 keV) using the Xspec flux tool. We calculated the flux of the blackbody model component using the Xspec model component cflux.

As in B20, we attempt to minimize differences in the NuSTAR and XMM-Newton response functions by not modeling the spectra from these telescopes in their overlapping energy ranges. As we discussed in B20, this introduces somewhat artificial inflation to the calibration constants between the spectra. The differences in cross-calibration are a known issue, albeit a poorly understood one, with the absolute calibration of XMM-Newton in Timing Mode (e.g., B20). These values should not be taken as a reflection of the relative fluxes seen by NuSTAR and XMM-Newton.

We do not present a spectral analysis of Observation R3 in this work, as it is presented with a comparable spectral model in Ramsay et al. (2002).

4. Results

4.1. Pulse Profiles

Her X-1's pulse profiles from Observations H1 and H4 (Figure 3) are somewhat similar in shape and relative phase. The hard NuSTAR profile has a strong, narrow main peak and a weaker, broader second peak. The soft XMM-Newton pulses have a broad, single-peaked structure. The main peaks of the hard and soft profiles are almost 180° out of phase in both Observation H1 and Observation H4.

The hard pulse profile from Observation R3 has a similar shape to the hard pulses in observations H1 and H4. However, the shape of the soft pulse changes, with the pulse steadily building strength up to the pulse maximum and then dropping

Table 3
Her X-1 Phase-averaged Spectral Parameters[a]

Parameter	Observation H1	Observation H2	Observation H3	Observation H4
$\mathrm{Flux_{total}}$ (erg $\mathrm{cm^{-2}\ s^{-1}}$; 0.3–60 keV)	$(6.418 \pm 0.006) \times 10^{-9}$	$(2.70 \pm 0.02) \times 10^{-10}$	$(9.72 \pm 0.03) \times 10^{-10}$	$(5.72 \pm 0.01) \times 10^{-9}$
$\mathrm{Flux_{power\ law}}$ (erg $\mathrm{cm^{-2}\ s^{-1}}$; 8–60 keV)[b]	$(4.559 \pm 0.005) \times 10^{-9}$	$(2.05 \pm 0.01) \times 10^{-10}$	$(7.67 \pm 0.02) \times 10^{-10}$	$(4.405 \pm 0.01) \times 10^{-9}$
$\mathrm{Flux_{blackbody}}$ (erg $\mathrm{cm^{-2}\ s^{-1}}$; 0.3–5 keV)	$(1.189 \pm 0.003) \times 10^{-10}$	$(2.54 \pm 0.03) \times 10^{-12}$	$(7.45 \pm 0.05) \times 10^{-12}$	$(9.18 \pm 0.06) \times 10^{-11}$
Photon Index	0.933 ± 0.004	0.56 ± 0.01	0.26 ± 0.01	0.933 ± 0.009
A_{powerlaw}	$(3.90 \pm 0.02) \times 10^{-2}$	$(1.30 \pm 0.03) \times 10^{-5}$	$(2.48 \pm 0.03) \times 10^{-5}$	$(3.34 \pm 0.03) \times 10^{-2}$
Cutoff Energy (keV)	19.8 ± 0.2	18.3 ± 0.4	17.8 ± 0.2	19.4 ± 0.4
Folding Energy (keV)	9.9 ± 0.2	9.0 ± 0.4	7.7 ± 0.2	9.7 ± 0.3
E_{CRSF} (keV)	36.5 ± 0.4	36 (fixed)	36 (fixed)	35.6 ± 0.7
σ_{CRSF} (keV)	5.1 ± 0.4	5 (fixed)	5 (fixed)	4.8 ± 0.7
CRSF Strength	6.6 ± 0.8	6.5 (fixed)	6.5 (fixed)	6 ± 2
kT_{BB} (keV)	0.0919 ± 0.0003	0.090 ± 0.001	0.0932 ± 0.0008	0.0884 ± 0.0006
A_{BB} (keV)	$(2.58 \pm 0.01) \times 10^{-3}$	$(5.7 \pm 0.1) \times 10^{-5}$	$(1.59 \pm 0.02) \times 10^{-4}$	$(2.09 \pm 0.02) \times 10^{-3}$
$E_{\mathrm{Fe\ K\alpha,\ broad}}$ (keV, fixed)	6.4	6.4	6.4	6.4
$\sigma_{\mathrm{Fe\ K\alpha,\ broad}}$ (keV, fixed)	0.5	0.5	0.5	0.5
$A_{\mathrm{Fe\ K\alpha,\ broad}}$ (photons $\mathrm{cm^{-2}\ s^{-1}}$)	$(1.00 \pm 0.09) \times 10^{-3}$	$(1.4 \pm 0.3)) \times 10^{-4}$	$(1.03 \pm 0.07) \times 10^{-3}$	$(1.27 \pm 0.2) \times 10^{-3}$
$E_{\mathrm{Fe\ K\alpha,\ narrow}}$ (keV, fixed)	6.4	6.4	6.4	6.4
$\sigma_{\mathrm{Fe\ K\alpha,\ narrow}}$ (keV, fixed)	0.1	0.1	0.1	0.1
$A_{\mathrm{Fe\ K\alpha,\ narrow}}$ (photons $\mathrm{cm^{-2}\ s^{-1}}$)	$(4.40 \pm 0.04) \times 10^{-4}$	$(5 \pm 2) \times 10^{-5}$	$(2.67 \pm 0.03) \times 10^{-4}$	$(2.3 \pm 0.8) \times 10^{-4}$
E_{bump} (keV, fixed)	0.9	0.9	0.9	0.9
σ_{bump} (keV, fixed)	0.191 ± 0.001	0.23 ± 0.01	0.243 ± 0.007	0.173 ± 0.003
A_{bump} (photons $\mathrm{cm^{-2}\ s^{-1}}$)	$(2.46 \pm 0.02) \times 10^{-2}$	$(5.6 \pm 0.3) \times 10^{-4}$	$(1.44 \pm 0.05) \times 10^{-3}$	$(1.58 \pm 0.04) \times 10^{-2}$
c_{FPMA}	2.58 ± 0.02	1.14 ± 0.02	1.06 ± 0.02	2.80 ± 0.04
c_{FPMB}	2.64 ± 0.02	1.16 ± 0.03	1.09 ± 0.02	2.85 ± 0.04
$c_{\mathrm{EPIC-pn}}$ (fixed)	1	1	1	1
χ^2	2172.01	1179.42	1993.86	872.82
Degrees of Freedom	1260	1035	1345	675

Notes.
[a] For the continuum model constant * tbnew * (powerlaw * highecut * gabs * gabs + bbody + Gauss + Gauss + Gauss). The errors on the flux are 1σ, and the errors on the parameters are 90% confidence intervals.
[b] We select 8–60 keV for the power-law flux because this energy range is consistent with the hard band used in our timing analysis.

off rapidly, as opposed to the rapid rise and slow decline of the pulses in Observations H1 and H4. There is also a change in the relative phase between the maxima of the hard and soft pulsations. The peaks of the hard and soft pulse profiles are separated by approximately 0.5 phase in Observations H1 and H4 and by approximately 0.2 phase in Observation R3.

The differences between these three pulse profiles demonstrate that the shape and relative phase of the soft pulses changes with the superorbital cycle. The similarity in the relative phase of the pulse profiles from Observations H1 and H4, which both take place around $\phi_{\mathrm{SO}} \approx 0.2$, shows that the pulses return to their original configuration after a complete precession cycle. However, if we create pulse profiles with finer binning, we can also see differences in the fine structure of the hard pulse profiles that arise from the difference in superorbital cycle between Observations H1 and H4 (e.g., Fürst et al. 2013; Staubert et al. 2013). In Figure 4, we show the hard-band pulse profile from Observations H1 and H4 made with 128 bins per phase. Both pulse profiles show a notch in the bright main pulse as well as structure within the interpulse. There are small differences in the fine structure of these profiles, which become even more noticeable in the energy-resolved pulse profiles in the Appendix, but these differences are consistent with expectations from the slightly different superorbital phase of these observations, based on the Staubert et al. (2013) template. Notably, Observation H4's interpulse contains two distinct bump-like features, where typically only one is observed; however, such fluctuations have been occasionally seen in Her X-1's pulse profiles with no obvious correlation to the superorbital phase (Staubert et al. 2013) . By showing simulated pulse profiles (see Section 5) in Figure 4 with a similar phase binning, we demonstrate that the warped disk model is not capable of reproducing the fine structure in the pulse profiles. For this reason, we use coarse-binned pulse profiles throughout our warped disk modeling procedure.

4.2. Spectroscopy

Our spectroscopic analysis indicates that an absorbed power law and soft blackbody component is a good description of the broadband X-ray continuum of Her X-1. Because Observations H1 and H4 capture a similar phase in the precession cycle of the inner disk, we expect that the spectra from these observations should also be similar. We do find several similarities in the spectral parameters (Table 3); the power-law parameters, including photon index, cutoff energy, and folding energy are consistent between the two observations. We also note that our fits for these two observations are consistent with those presented in Staubert et al. (2020). There are some small differences between the blackbody temperature and strength or normalization of the emission-line components between these two observations. These differences are expected given the small difference in flux between these observations, which can be seen in the difference between pulse profile count rates in Observations H1 and H4 (see Figure 3).

Our spectral fits to Observations H2 and H3 show some distinct differences in the power-law shape from Observations H1 and H4. Although some difference in spectral shape with the superorbital phase is expected (Fürst et al. 2013), Observations H2 and H3 have significantly lower flux than Observations H1

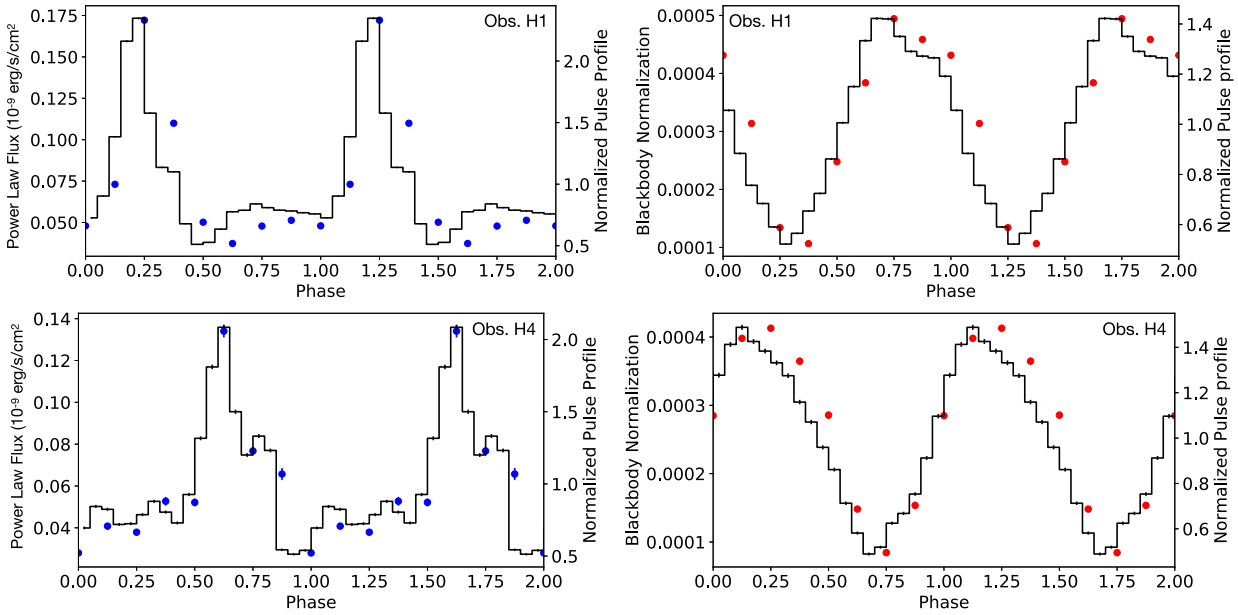

Figure 6. Left: power-law flux (8–60 keV, blue points) compared to the NuSTAR 8–60 pulse profile for Observation H1 (top row, $\phi_{SO} = 0.20$) and Observation H4 (bottom row, $\phi_{SO} = 0.14$). Right: blackbody normalization (red points) compared to the XMM-Newton 0.3–0.7 keV pulse profile for Observations H1 (top row) and H4 (bottom row). In both cases, the phase-resolved spectroscopy parameters are in good agreement with their respective pulse profiles. The agreement between the spectral parameters and their respective energy-resolved pulse profiles demonstrates that the pulse profiles are a suitable proxy for their respective flux parameters in our warped disk model.

and H4. This is consistent with the obscuration of the neutron star by the accretion disk, which would also explain other features of these observations, including the differences in spectral continuum shape and pulse strength (Deeter et al. 1998; Leahy 2000). Increased obscuration could also explain the weakened CRSF present in Observations H2 and H3, as the reduced flux of the entire spectrum would make this feature more difficult to detect. The nondetection of the CRSF at low flux is supported by previous work by İnam & Baykal (2005), who did not find a CRSF feature necessary to fit the low-state spectrum of Her X-1.

5. Modeling the Warped Inner Disk

To constrain the geometry of the inner accretion disk during its precession, we used the same model as B20, which was first presented in Hickox & Vrtilek (2005). A full description of the model, its underlying assumptions, and a schematic diagram can be found in B20. We briefly describe an important assumption here for clarity.

A fundamental assumption of the B20 warped disk model is that the emission below 1 keV follows the blackbody emission of the accretion disk and that hard X-ray emission follows the power law. We demonstrate this relationship by performing a simplistic phase-resolved spectral analysis. For Observations H1 and H4, where strong pulsations were detected, we used the HENDRICS tool HENphasetag to assign pulse phase values to each photon in the NuSTAR and XMM-Newton event files. We then filtered the data into eight equal phase bins using xselect for NuSTAR data and evselect for XMM-Newton data. We extracted spectra and grouped them with a minimum of 100 counts per bin. We modeled the joint phase-resolved spectra between 0.3–47 keV due to the poorer statistics in these spectra.

We attempted to use the phase-averaged spectral model to also describe the phase-resolved spectra, but the reduced signal to noise in the phase-resolved spectra required that we reduce degeneracy between some model parameters. We fixed the blackbody temperature, the width of the CRSF, and the width of the 0.9 keV bump feature to their phase-averaged values. We also removed the broad iron line model component and only used the narrow emission line at 6.4 keV. This simplified spectral model allowed us to evaluate the changes in the blackbody and power-law normalizations.

In Figure 6, we show the power-law flux and the NuSTAR 8–60 keV pulse profile as well as the blackbody normalization compared to the XMM-Newton 0.3–0.7 keV pulse profile from Observation H1. Both the hard and the soft pulses show good phase agreement. The good agreement between the integrated flux in this energy range and their respective pulse profiles demonstrates that we can use the pulse profiles as a suitable proxy for the spin-resolved power-law and blackbody flux. Using this proxy, we can use the warped disk model to simulate the energy-resolved XMM-Newton and NuSTAR pulse profiles and assume that the profiles follow any changes in the respective strength of the blackbody and power law.

With this relationship verified, we will now describe the warped disk model itself. This model uses a simple warped disk geometry, represented by a series of concentric circles that are tilted and twisted relative to one another, to describe the inner accretion disk. The disk is defined by the radius and tilt angle of the inner (r_{in}, θ_{in}) and outer (r_{out}, θ_{out}) rings and their relative twist angle with respect to one another (θ_{tw}). The height of the observer is set by the observer angle (θ_{obs}).

The pulsar emission geometry can be represented either as a narrow pencil beam or by a wider fan beam. The beam geometry consists of two beams, whose locations on the neutron star surface are defined by θ_b and ϕ_b, which are the angle out of the rotational plane and the azimuthal angle, respectively. The pencil-beam profile is a two-dimensional Gaussian with width σ_b. The

Table 4
Disk Model Parameters

Parameter	Observation H1		Observation R3		Observation H4	
	Pencil Beam	Fan Beam	Pencil Beam	Fan Beam	Pencil Beam	Fan Beam
r_{in} (10^8 cm)	0.8	0.8	0.8	0.8	0.8	0.8
r_{out} (10^8 cm)	1	1	1	1	1	1
Inner tilt θ_{in} (deg)	10	10	10	10	10	10
Outer tilt θ_{out} (deg)	30	30	30	30	30	30
Twist angle ϕ_{tw} (deg)	139	139	139	139	139	139
$Beam_1$ angle from rotational plane θ_{b1} (deg)	0	40	0	40	0	40
$Beam_2$ angle from rotational plane θ_{b2} (deg)	60	60	60	60	60	60
$Beam_1$ azimuth ϕ_{b1} (deg)	0	0	0	0	0	0
$Beam_2$ azimuth ϕ_{b2} (deg)	210	140	220	130	210	140
Beam half-width σ_b (deg)	45	60	45, 60[a]	60	45	60
Fan-beam opening angle θ_{fan} (deg)	0	60	0	60	0	60
Observer elevation θ_{obs} (deg)	−5	−5	−5	−5	−5	−5

Note.
[a] Here the beam widths were asymmetric, with $\sigma_{b1} = 45°$ and $\sigma_{b2} = 60°$.

fan beam is also a two-dimensional Gaussian with an additional opening angle (θ_{fan}).

Once the disk and emission geometry are specified, the model calculates the simulated pulse profile at 30 pulse phases and 8 disk precession angles. As the pulsar rotates, the beam profile irradiates the inner accretion disk. The hard pulse profile is made by calculating the luminosity of the beam visible to the observer as a function of pulse phase and disk precession angle. We generate the soft pulse profile by calculating the luminosity of the irradiated disk visible to the observer. We then compare the simulated pulse profiles to the observed profiles. This model does not include the effects of general relativity or light bending.

When modeling Her X-1's inner disk, we are able to use previous models of Her X-1's warped disk to guide our choice of parameters. Scott et al. (2000) created a model disk that would reproduce observed changes in Her X-1's observed pulse profiles between the main on and short on of the superorbital cycle. They used a low observer elevation consistent with the high inclination of the source ($\theta_{obs} = -5°$) and defined the disk as having an inner tilt angle (θ_{in}) of 11° and an outer tilt angle (θ_{out}) of 20°. Furthermore, they used a twist angle of 139° between the inner and outer rings of the disk. Similar parameters were used by Leahy (2002), who created a warped disk to reproduce the observed 35 day superorbital modulation as seen by RXTE. Leahy (2002) found that an observer angle of 5° and an outer tilt angle of 30° best reproduced the shape of the superorbital cycle. For this work, we adopted the disk parameters found by Scott et al. (2000) and used an observer elevation of −5°. We also tried using the Scott et al. (2000) outer disk tilt angle of 20° but ultimately found a better fit to our observed pulse profiles with the Leahy (2002) value of 30°. Our full set of model parameters is shown in Table 4.

We kept the disk geometry set to the values described above for all three observations. We allowed the location of the two beams and their widths to vary until we matched the observed shape of the hard pulse profiles (Table 4). We allowed the model disk to precesss around the pulsar, which changed the shape and phase of the soft pulse profile component. We calculated the simulated hard and soft pulse profiles at eight equally spaced disk precession angles. We then fit the simulated pulse profile to the observed pulse profile, allowing the overall amplitude of the simulated pulsations to scale, and estimated the goodness of fit by calculating $r = \sum(P_{obs}(\phi_{spin}) - P_{sim}(\phi_{spin}))/\sqrt{P_{obs}}$, where P_{obs} is the observed pulse profile and P_{sim} is the simulated pulse profile. The disk precession phase with the lowest r value represents the orientation of the disk that reproduces the observed pulsations best, and these phases are highlighted in green in Figures 7 and 8. We performed the fits for the pencil- and fan-beam configurations independently.

Because the energy-resolved pulse profiles for Observation H1 and Observation H4 are extremely similar, the best-fit beam geometry and disk precession angle are the same in both observations. The disk precession angle of 0.25 closely matches the superorbital phase of Observations H1 and H4 ($\phi_{SO} \approx 0.2$). In Observation R3, the disk precession angle that best reproduced the observed pulse profiles was slightly off, at angle 0.75 rather than the closer value of 0.625. We are encouraged by the fact that the model came close to selecting the correct phase bin, especially considering that Observation R3 occurred almost 18 yr before Observations H1 and H4. We show the model disks that produced our best-fit simulated pulse profiles in Figure 9 and list the parameters for the disk and beam geometries in Table 4.

6. The Pre-eclipse Dip

Observation H4 captured a pre-eclipse dip with both NuSTAR and XMM-Newton, as seen in the light curve in Figure 2. This observation began at 58556.278576 MJD and ended at 58556.750799 MJD, with the next eclipse occurring at 58556.874225 MJD. Giacconi et al. (1973) noted the presence of pre-eclipse dips in long-term UHURU light curves of Her X-1. During these dips, the flux of Her X-1 drops significantly as most of the pulsating emission becomes heavily absorbed (Giacconi et al. 1973; Stelzer et al. 1999). The unabsorbed emission spectrum is well described by a power law, suggesting that this persistent emission results from X-ray scattering in the obscuring material (Vrtilek & Halpern 1985; Choi et al. 1994; Leahy et al. 1994; Reynolds & Parmar 1995). Modeling of long-term X-ray light curves suggests that these dips are caused by obscuration of material at the impact region of the accretion stream and accretion disk (e.g., Igna & Leahy 2012).

This dip presented an opportunity to examine the onset of the dip as a function of energy across a wide range of X-ray energies. In Figure 10, we show energy-resolved light curves of

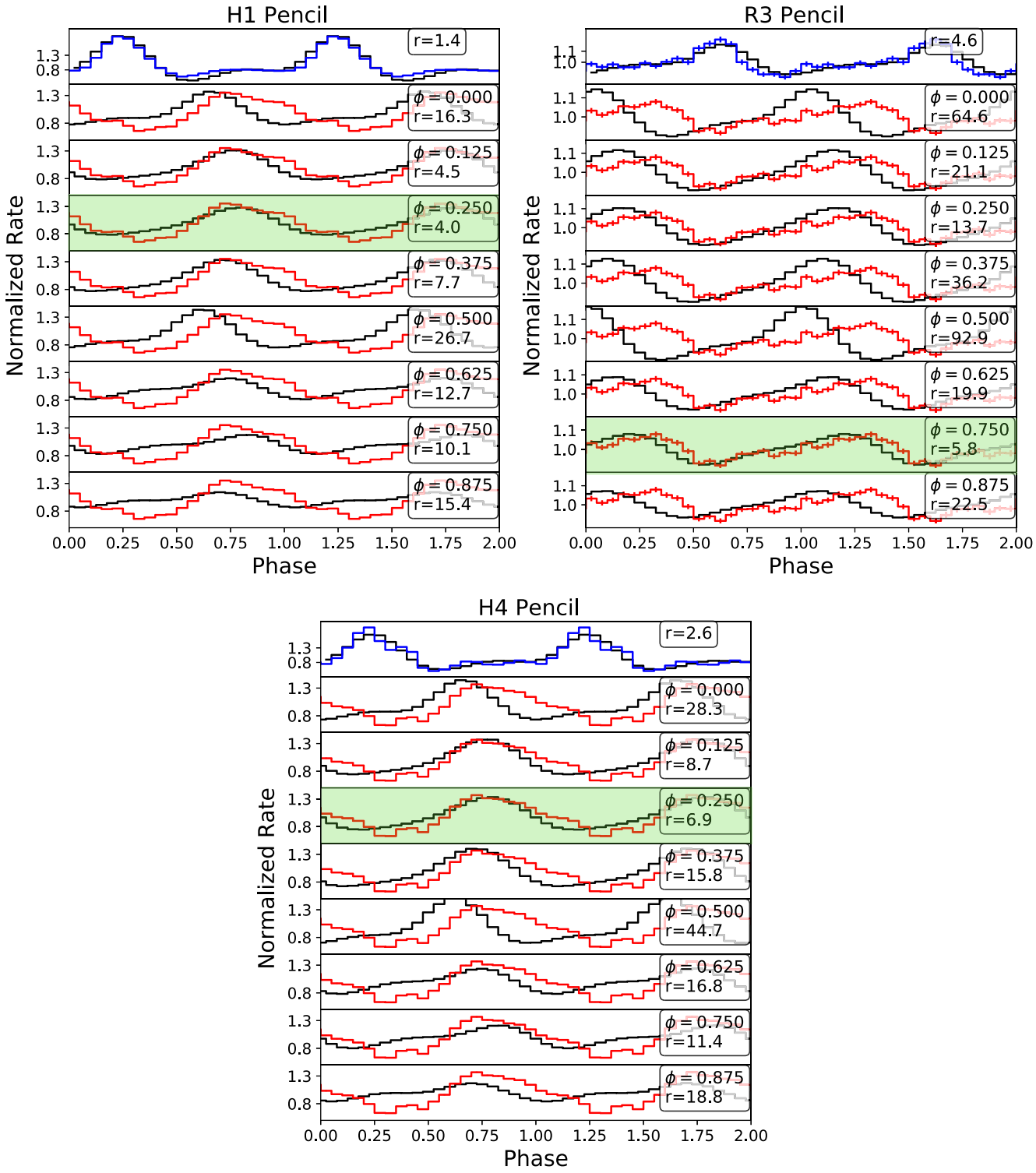

Figure 7. Observed hard (blue) and soft (red) pulse profiles compared with simulated (black) pulse profiles from the warped disk model with a pencil beam for the three Her X-1 observations. The disk precession angles (ϕ) correspond to the 35 day superorbital phase. For each disk precession angle, we calculate the goodness of fit with the parameter r ($r = \sum(P_{\rm obs}(\phi_{\rm spin}) - P_{\rm sim}(\phi_{\rm spin}))/\overline{P_{\rm obs}}$, where $P_{\rm obs}$ is the observed pulse profile and $P_{\rm sim}$ is the simulated pulse profile). For the soft pulses, a disk precession of $\phi_{\rm SO} = 0.25$ (highlighted in green) best describes the observed pulse profiles of Observations H1 and H4, while a disk precession of $\phi_{\rm SO} = 0.75$ best describes Observation R3.

the onset of the dip, binned by 30 s. In the soft (0.5–1 keV) X-rays, the transition from bright to faint emission is almost immediate, taking place in a single 30 s time bin. In the middle (7–12 keV) and hard (15–60 keV) X-rays, the transition occurs more slowly, over hundreds of seconds. The varying response of the energy-resolved light curves is consistent with the

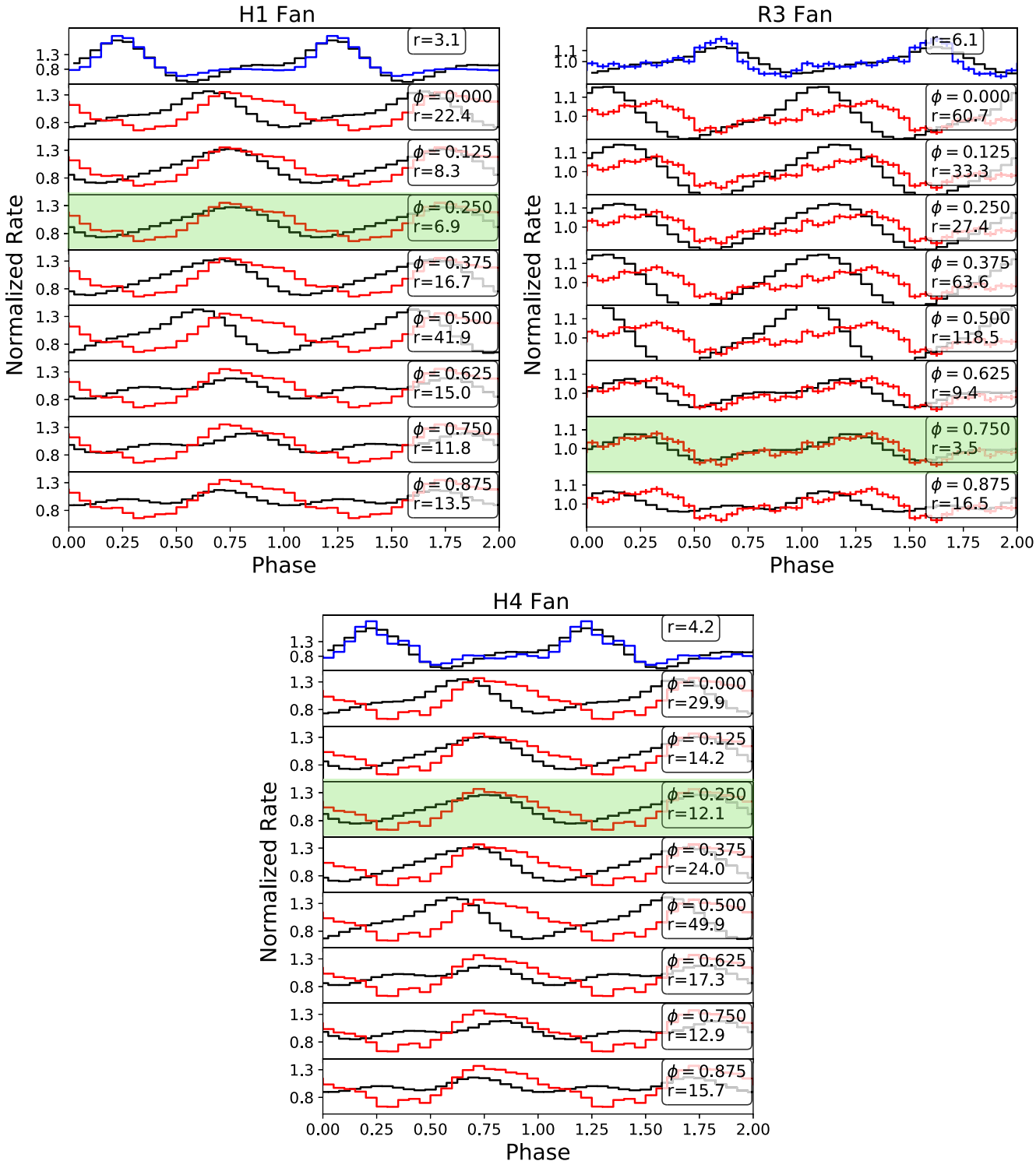

Figure 8. Observed hard (blue) and soft (red) pulse profiles compared with simulated (black) pulse profiles from the warped disk model with a fan beam for the three Her X-1 observations. The disk precession angles (ϕ) correspond to the 35 day superorbital phase. For each disk precession angle, we calculate the goodness of fit with the parameter r ($r = \sum(P_{\rm obs}(\phi_{\rm spin}) - P_{\rm sim}(\phi_{\rm spin}))/\overline{P_{\rm obs}}$, where $P_{\rm obs}$ is the observed pulse profile and $P_{\rm sim}$ is the simulated pulse profile). For the soft pulses, a disk precession of $\phi_{\rm SO} = 0.25$ (highlighted in green) best describes the observed pulse profiles of Observations H1 and H4, while a disk precession of $\phi_{\rm SO} = 0.75$ best describes Observation R3.

generally held picture of an increase in absorber column density and scattering of the hard X-ray continuum (e.g., Vrtilek & Halpern 1985; Leahy et al. 1994).

The black arrow in Figure 10 marks a short rebrightening event seen during the onset of the pre-eclipse dip in the higher energy X-ray bands. This event could be related to the "spike" phenomenon first seen by Vrtilek & Halpern (1985), where short increases in X-ray luminosity were seen during Her X-1's pre-eclipse dips. Vrtilek & Halpern (1985) reported that these spikes reached as much as 80% of the

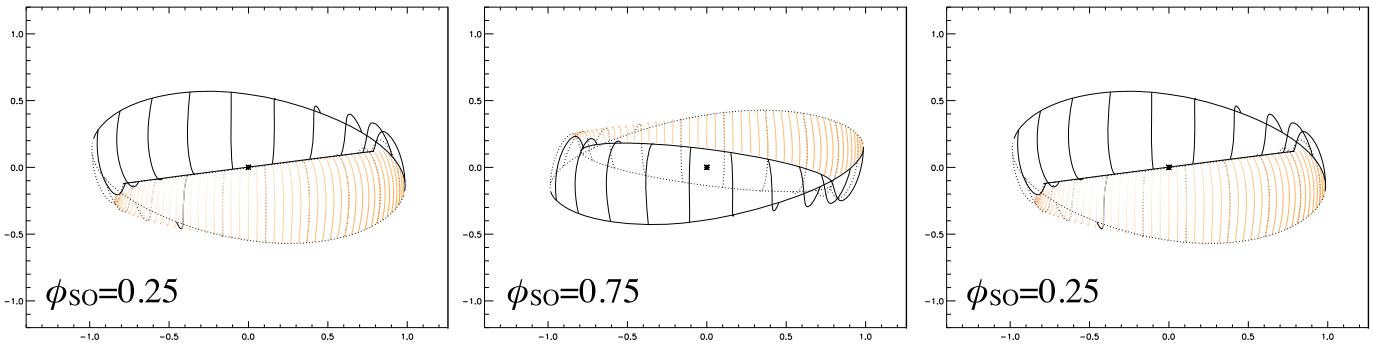

Figure 9. The simulated disk that best reproduces the observed pulse profiles from Observations H1, R3, and H4 for both the fan-beam and pencil-beam models. The orange shaded section of the disk represents the illuminated side of the disk, while black lines indicate the back of the disk, which is not illuminated by the pulsar beam. Units are 10^8 cm.

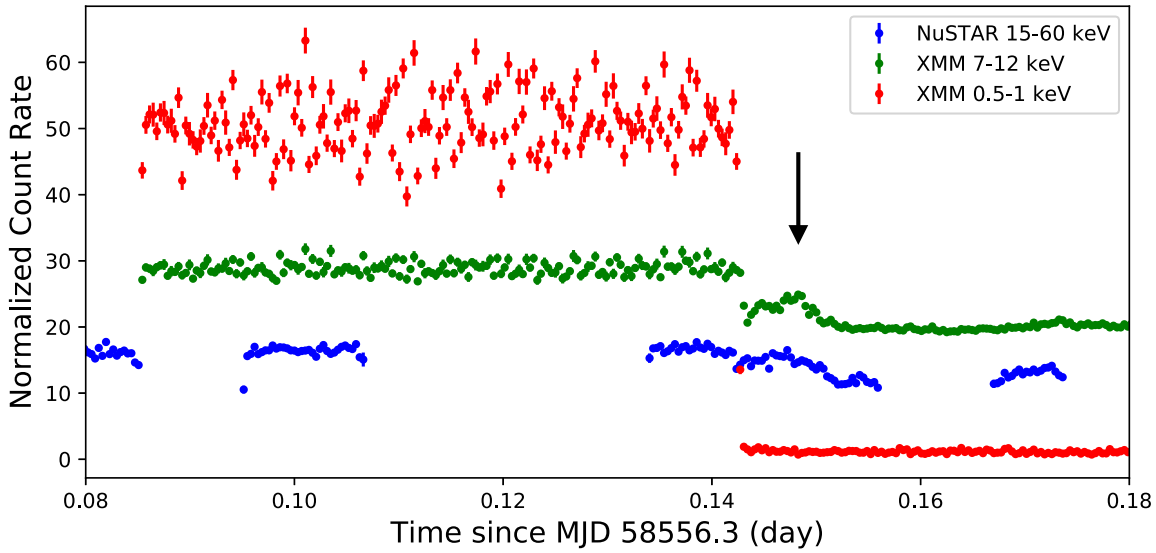

Figure 10. Energy-resolved light curves centered around the onset of the pre-eclipse dip in Observation H4 and binned with 30 s bins. The transition is abrupt in the soft X-rays (0.5–1 keV, red) and more gradual in the mid (7–12 keV, green) and hard (15–60 keV, blue) curves. The black arrow marks a rebrightening event during the onset of the dip that is visible in the higher energy bands. The count rates for each light curve have been arbitrarily offset for clarity. We cleaned the XMM-Newton light curves using the SAS tool epiclccorr to remove bins with low exposure fraction due to Counting Mode.

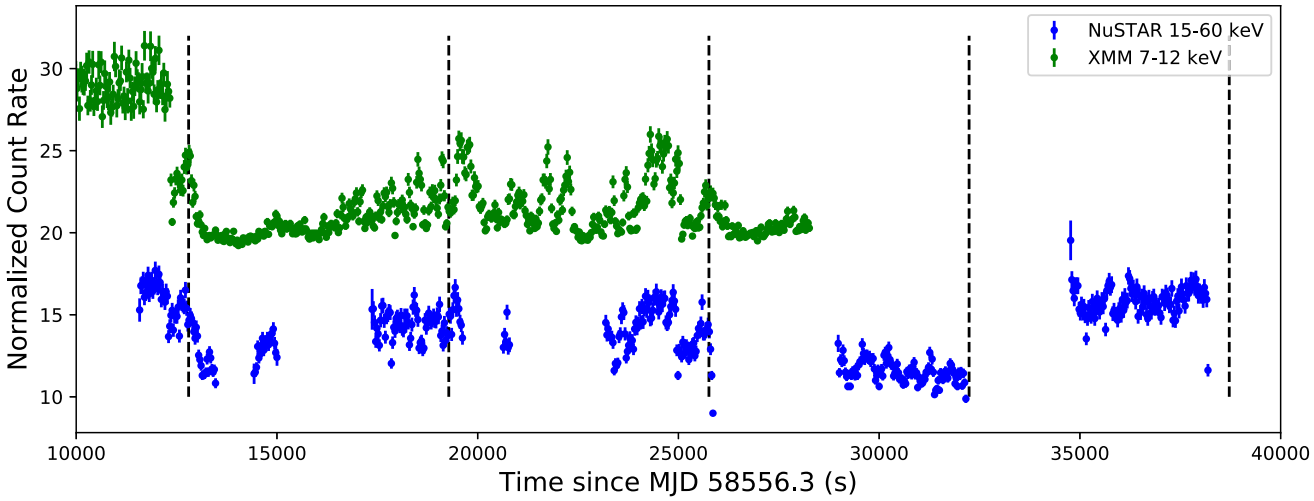

Figure 11. The same middle (7–12 keV, green) and hard (15–60 keV, blue) light curves from Figure 10, but shifted in time to focus on the dip, rather than its onset. The onset of the dip starts at 12,000 s in this plot. The black dashed lines are placed at 108 minute intervals, starting at the first rebrightening event during the onset of the dip. The activity seen in this pre-eclipse dip does not appear to follow a 108 minute period.

pre-dip flux, lasted about 5–8 minutes, and repeated with a period of 108 minutes.

While the soft (0.5–1 keV) energy band is mostly obscured during the pre-eclipse dip, we do see variations in brightness within the dip in the middle (7–12 keV) and hard (15–60 keV) energy bands, which we show in Figure 11. We performed an epoch-folding search of the dip light curve to check for periodic behavior and found no significant periods within the pre-eclipse dip.

To further check for the 108 minute period found by Vrtilek & Halpern (1985), we included vertical dashed lines in Figure 11 at 108 minute intervals starting with the rebrightening event marked with the black arrow in Figure 10. While the first, second, and third intervals do align with some variations in the light curve, there is significantly more variation present than can be described with a 108 minute period. Additionally, the variations we see in this dip appear less pronounced than those seen by Vrtilek & Halpern (1985).

While we do not see the clear spiking phenomenon observed by Vrtilek & Halpern (1985), we do see significant variability in the hard X-ray flux during the pre-eclipse dip. This variability seems consistent with that observed by Leahy et al. (1994) and could possibly be caused by irregularities in the structure of the obscuring material. We leave a more detailed analysis of the variations seen in Observation H4 and their spectral similarity to the spikes of Vrtilek & Halpern (1985) to a later analysis.

7. Discussion

Several previous works, including McCray et al. (1982), Scott et al. (2000), Leahy (2002), Ramsay et al. (2002), Zane et al. (2004), Hickox et al. (2004), Kuster et al. (2005), and Staubert et al. (2013), suggested that the changes in pulse profile shape with superorbital phase in Her X-1 were caused by reprocessing in the inner accretion disk during its precession around the neutron star. In this work, we use three observations of Her X-1 at different superorbital phases to show that the observed changes in pulse profile shape and relative phase can be modeled by a simple precessing accretion disk.

If disk precession is the cause of the changes in shape and phase of the pulse profiles, then we expect that observations from the same superorbital phase should have similar pulse profile shapes. We confirm this expectation with the Observation H1 and H4 pulse profiles, which have similar pulse shapes and the same relative phase offset between the hard and soft pulsations. These results are strengthened by good agreement with archival data of Her X-1, particularly the NuSTAR pulse profiles presented in Fürst et al. (2013) from superorbital phases 0.11 and 0.17, which show a similar pulse shape to H1 and H4.

We also expect to see periodicity in the spectral continuum with the superorbital cycle in the precessing disk scenario. In our joint XMM-Newton and NuSTAR spectral analysis, we do see similarities between Observations H1 and H4, particularly in the high-energy continuum (photon index, power-law cutoff, and folding energies), the shape of the CRSF, and the size of the soft bump feature (e.g., Jimenez-Garate et al. 2002; Fürst et al. 2013). We do find some differences in the blackbody temperature and normalization between Observations H1 and H4, which is likely due to a combination of the short pre-dip exposure time for Observation H4 and small changes in the spectral continuum shape with superorbital phase (e.g., Fürst et al. 2013).

We see significantly different spectral shapes in Observations H2 and H3 than we do in H1 and H4. While some spectral differences with the superorbital phase are to be expected, the low flux and lack of strong pulsations during Observations H2 and H3 indicate that these observations are somewhat unusual for Her X-1. We suggest that the neutron star and central accretion region were obscured during these observations because of the reduced flux and lack of pulsations.

Using the same warped disk model from B20, we were able to simulate a simple warped disk irradiated by either a pencil- or a fan-beam emission geometry and calculate the simulated pulse profiles that would be observed for different precession angles of the disk. We used the previous disk modeling of Scott et al. (2000) and Leahy (2002) to guide our choice of disk geometry. We ultimately found that both the pencil- and fan-beam emission models, which were fit independently, were capable of reproducing the observed pulse profiles and that the simulated disk precession phase was in good agreement with the superorbital phase of our observations. However, the pencil-beam emission geometry provides a slightly better fit to the observed pulse profiles, which can be seen by the smaller values of r for each observation in Figures 7 and 8. However, we would like to note that the geometries used in this model are simplistic for the purpose of highlighting the contribution of the precessing disk. It is likely that the accretion geometry of Her X-1 is more complex than this model suggests.

In both the fan- and pencil-beam emission geometries, we find that the preferred beam geometry is strongly non-antipolar. We demonstrate this conclusion by showing a simulated pulse profile from antipodal pencil beams in Figure 4. The shape of the simulated pulse profile from antipodal beams is not a good fit to our observed pulse profiles. Kraus et al. (1995) identified distortions in the dipolar field of neutron stars as a possible cause of asymmetry in pulse profiles. Blum & Kraus (2000) found that the energy-resolved pulse profiles from Her X-1 suggested a slightly distorted dipolar field. B20 and Hickox & Vrtilek (2005) also found this preference for non-antipolar beams. This preference may suggest that the structure of magnetized accretion flows are more complex than the current scope of our warped disk model. Future modeling efforts would benefit from considering more complex emission geometries (e.g., Koliopanos & Vasilopoulos 2018; Iwakiri et al. 2019), physically motivated accretion column models (e.g., E. Sokolova-Lapa 2021, in preparation), or the effects of light bending from the neutron star (e.g., Falkner 2021a, 2021b).

Observation H4 contains a pre-eclipse dip from Her X-1 with both XMM-Newton and NuSTAR. Examining the pulsed fractions (Figure 2) and energy-resolved light curves (Figure 10) both show strong absorption of the soft X-ray emission consistent with obscuration by part of the accretion disk. The data do not show evidence of a periodic spiking signal previously seen by Vrtilek & Halpern (1985).

8. Conclusion

In this work, we performed a broadband X-ray timing analysis of Her X-1 during its 35 day superorbital cycle. Our series of four joint XMM-Newton and NuSTAR observations sampled a single superorbital cycle; however, we focus on the first and fourth observations in this series, which had sufficient signal to noise to create energy-resolved pulse profiles in

narrow energy bandpasses. We supplemented our missing coverage of the superorbital phase with an archival XMM-Newton observation at $\phi_{SO} = 0.60$. We found that the soft (<1 keV) and hard (>8 keV) pulse profiles had similar shapes and relative phase offsets in Observations H1 and H4, which we expected from a warped, precessing accretion disk that has returned to its original position. The joint spectral fits also showed periodicity with the superorbital phase, which supports the precessing disk scenario. We use the simple warped disk model used by B20 to simulate our observed pulse profiles and find that they are consistent with reflection off of a precessing disk. We find a strong preference for non-antipolar neutron star beam geometry, which is consistent with the results of B20. Updates to this model with more physically motivated beam geometries could further test this non-antipolar preference. We also examined the energy-resolved light curves of the pre-eclipse dip seen in Observation H4. We find strong absorption of the soft X-rays and variability in the hard X-rays consistent with previous observations. We do not see evidence of a periodic signal within the dip.

We would like to thank the anonymous referee for comments and suggestions that greatly improved the clarity and substance of this paper. We thank Lorenzo Ducci and Matteo Bachetti for helpful discussions relating to the spectral and timing analyses, respectively. We would like to thank the NuSTAR Galactic Binaries Science Team for comments and contributions. M.C.B. acknowledges support from NASA grant numbers NNX15AV32G and NNX15AH79H. This research made use of NuSTARDAS, developed by ASDC (Italy) and Caltech (USA), XMM-SAS developed by ESA, ISIS functions (ISIS-scripts) provided by ECAP/Remeis observatory and MIT (http://www.sternwarte.uni-erlangen.de/isis/), and the MAXI data provided by RIKEN, JAXA, and the MAXI team.

Software: HEAsoft (v6.26.1; HEASARC 2014), NuSTARDAS, SAS (Gabriel et al. 2004), Stingray (Huppenkothen et al. 2019), Xspec (v12.10.1; Arnaud 1996), MaLTPyNT (Bachetti 2015).

Appendix
Extended Timing Analysis

Although we could not use our warped disk model on Observation H3 due to the lack of XMM-Newton pulsations, we were able to extract a NuSTAR 8–60 keV pulse profile. To create this pulse profile, we selected the first 5 ks of NuSTAR data which were most strongly pulsed and followed the method described in Section 3. We show the NuSTAR pulse profile of Observation H3 in Figure 12. The pulse profile shows a single broad peak that is atypical for hard pulses from Her X-1.

When selecting the energy bands to be used in our hard and soft pulse profiles, we found it necessary to examine the energy dependence of the pulse profile to make an appropriate selection. This decision was motivated heavily by Ramsay et al. (2002), who examined the energy dependence of their XMM-Newton observations and found changes in the soft pulse profile beginning around 0.8 keV (see Figure 2 in Ramsay et al. (2002). We created similar figures by filtering the XMM-Newton data for Observations H1 and H4 into the following energy bins: 0.3–0.7 keV, 0.8–1.2 keV, 1.5–3 keV, 3–6 keV, 6.2–6.6 keV, and 7–12 keV. We also filtered the NuSTAR data for Observations H1 and H4 into energy bins consisting of 3–6 keV, 6.2–6.6 keV, 7–12 keV, 12.4–30 keV, and 30.4–60 keV. We based these energy bins on those used by Ramsay et al. (2002) but adjusted the energy ranges slightly to suit joint XMM-Newton and NuSTAR observations. We also filtered the pulsed portion of the NuSTAR data from Observation H3 into the same energy bands used for the NuSTAR data of Observations H1 and H4. As mentioned in Section 2, we were unable to extract coherent energy-resolved pulse profiles from the XMM-Newton data of Observation H3.

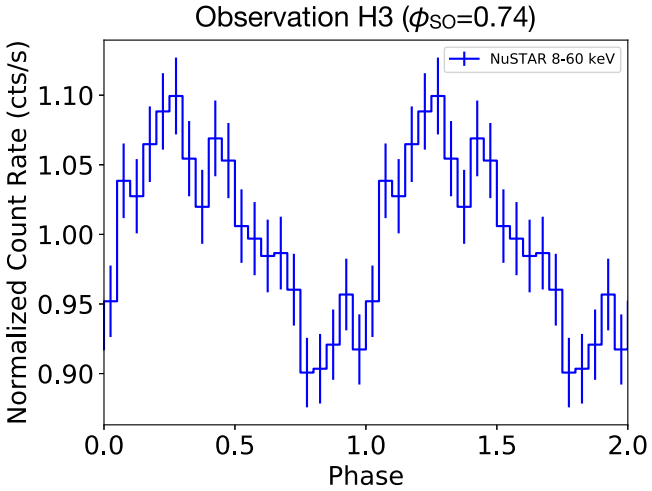

Figure 12. The NuSTAR 8–60 keV pulse profile from the first 5 ks of Observation H3. The pulses in this observation are weaker and have a different pulse shape than those seen in Observations H1 and H4. For clarity, we have shifted this pulse profile so that the peak aligns in phase with the hard peak from Observation H1.

We folded the energy-resolved data by the best-fit period for the corresponding observation. We varied the resolution with which we plotted the pulse profiles to match the effective exposure of the pulsed emission from each observation: Observation H1 profiles contain 128 phase bins, Observation H3 profiles contain 20 phase bins, and Observation H4 profiles contain 70 phase bins. We have also shifted the profiles of Observations H3 and H4 so that the hard pulse peak aligns in phase with the peak from H1. We show the resulting pulse profiles in Figure 13.

Figure 13 shows that the soft pulse profiles are highly energy dependent and that the sharp, notched peak that defines the hard pulse profile begins to emerge around 0.8 keV. In order to isolate the soft, reprocessed emission, we therefore selected the energy range of 0.3–0.7 keV for our soft energy band in this work.

While the pulse profiles of Observations H1 and H4, and their energy dependence, are almost identical (as we expect from the precessing disk scenario), the pulse profiles from Observation H3 differ significantly. The pulsations are generally weaker and the pulse is much broader than the pulses in Observations H1 and H4, and lacks the distinctive notch. Some differences in pulse shape can be expected from the processing disk scenario, in which different parts of the accretion column are visible at this superorbital phase.

Interestingly, we note that the energy-resolved pulse profiles shown by Ramsay et al. (2002) are significantly different in shape than those from our series, despite the similar energy bins used. Some of these changes may be expected from the differences in the superorbital phase (Ramsay et al. 2002 observations fall at superorbital phases 0.17, 0.26, and 0.60, compared to the phases of Observations H1, H3, and H4 of

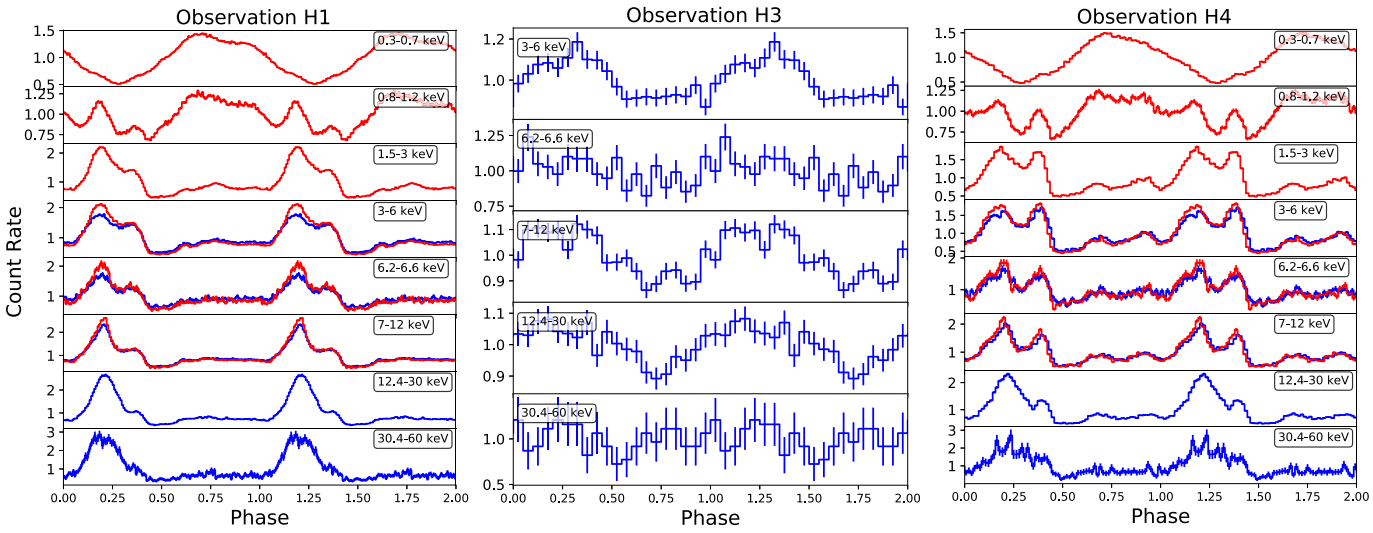

Figure 13. Energy-resolved pulse profiles for Observations H1, H3, and H4. Red profiles are XMM-Newton and blue profiles are NuSTAR. In order to show the pulse profiles in detail while maintaining a high signal-to-noise ratio, we varied the resolution with which we produced these profiles to match the effective exposure of the pulsed emission: Observation H1 profiles contain 128 phase bins, Observation H3 profiles contain 20 phase bins, and Observation H4 profiles contain 70 phase bins. We have also shifted the profiles of Observations H3 and H4 so that the hard pulse peak aligns in phase with the peak from H1, for clarity. We note that there is strong energy dependence in the soft band, which is illustrated by the emergence of the primary pulse peak as early as 0.8 keV. The softest energy band (0.3–0.7 keV) shows a smooth, single-peaked profile that we expect from reprocessed emission (e.g., Hickox et al. 2004). The 0.8–1.2 keV band appears to be a mix of the reprocessed emission and the harder, sharply pulsed profiles that dominate at energies above 1.5 keV. In Observation H3, we are unable to produce energy-resolved pulse profiles from the XMM-Newton data.

0.20, 0.74, and 1.14). However, the magnitude of these differences implies that the pulse shape has changed between these two series. The pulse profiles shown in this work show more similarity to the pulse profiles presented in Staubert et al. (2009).

ORCID iDs

McKinley C. Brumback https://orcid.org/0000-0002-4024-6967
Ryan C. Hickox https://orcid.org/0000-0003-1468-9526
Felix S. Fürst https://orcid.org/0000-0003-0388-0560
Katja Pottschmidt https://orcid.org/0000-0002-4656-6881
John A. Tomsick https://orcid.org/0000-0001-5506-9855
Jörn Wilms https://orcid.org/0000-0003-2065-5410
Rüdiger Staubert https://orcid.org/0000-0003-1498-1543
Saeqa Vrtilek https://orcid.org/0000-0002-7521-9897

References

Arnaud, K. A. 1996, in ASP Conf. Ser. 101, Astronomical Data Analysis Software and Systems, ed. G. H. Jacoby & J. Barnes (San Francisco, CA: ASP), 17
Bachetti, M. 2015, MaLTPyNT: Quick look timing analysis for NuSTAR data, Astrophysics Source Code Library, ascl:1502.021
Bala, S., Bhattacharya, D., Staubert, R., & Maitra, C. 2020, MNRAS, 497, 1029
Blum, S., & Kraus, U. 2000, ApJ, 529, 968
Brumback, M. C., Hickox, R. C., Fürst, F. S., et al. 2020, ApJ, 888, 125
Buccheri, R., Bennett, K., Bignami, G. F., et al. 1983, A&A, 128, 245
Choi, C. S., Nagase, F., Makino, F., Dotani, T., & Min, K. W. 1994, ApJ, 422, 799
Coburn, W., Heindl, W. A., Rothschild, R. E., et al. 2002, ApJ, 580, 394
Coburn, W., Heindl, W. A., Wilms, J., et al. 2000, ApJ, 543, 351
Crampton, D., & Hutchings, J. B. 1974, ApJ, 191, 483
Deeter, J. E., Boynton, P. E., & Pravdo, S. H. 1981, ApJ, 247, 1003
Deeter, J. E., Scott, D. M., Boynton, P. E., et al. 1998, ApJ, 502, 802
Falkner, S. 2021a, A&A, submitted
Falkner, S. 2021b, A&A, submitted
Fürst, F., Grefenstette, B. W., Staubert, R., et al. 2013, ApJ, 779, 69
Gabriel, C., Denby, M., Fyfe, D. J., et al. 2004, in ASP Conf. Ser. 314, Astronomical Data Analysis Software and Systems (ADASS) XIII, ed. F. Ochsenbein, M. G. Allen, & D. Egret (San Francisco, CA: ASP), 759
Gerend, D., & Boynton, P. E. 1976, ApJ, 209, 562
Giacconi, R., Gursky, H., Kellogg, E., et al. 1973, ApJ, 184, 227
Gruber, D. E., Heindl, W. A., Rothschild, R. E., et al. 2001, ApJ, 562, 499
Harrison, F. A., Craig, W. W., Christensen, F. E., et al. 2013, ApJ, 770, 103
Heemskerk, M. H. M., & van Paradijs, J. 1989, A&A, 223, 154
Hickox, R. C., Narayan, R., & Kallman, T. R. 2004, ApJ, 614, 881
Hickox, R. C., & Vrtilek, S. D. 2005, ApJ, 633, 1064
HI4PI Collaboration, Ben Bekhti, N., Flöer, L., et al. 2016, A&A, 594, A116
Huppenkothen, D., Bachetti, M., Stevens, A. L., et al. 2019, ApJ, 881, 39
Igna, C. D., & Leahy, D. A. 2012, MNRAS, 425, 8
İnam, S. C., & Baykal, A. 2005, MNRAS, 361, 1393
Iwakiri, W. B., Pottschmidt, K., Falkner, S., et al. 2019, ApJ, 878, 121
Jimenez-Garate, M. A., Hailey, C. J., den Herder, J. W., Zane, S., & Ramsay, G. 2002, arXiv:astro-ph/0202109
Jones, C., & Forman, W. 1976, ApJL, 209, L131
Joye, W. A., & Mandel, E. 2003, in ASP Conf. Ser. 295, Astronomical Data Analysis Software and Systems XII, ed. H. E. Payne, R. I. Jedrzejewski, & R. N. Hook (San Francisco, CA: ASP), 489
Koliopanos, F., & Vasilopoulos, G. 2018, A&A, 614, A23
Kraus, U., Nollert, H. P., Ruder, H., & Riffert, H. 1995, ApJ, 450, 763
Kuster, M., Wilms, J., Staubert, R., et al. 2005, A&A, 443, 753
Leahy, D. A. 2000, MNRAS, 315, 735
Leahy, D. A. 2002, MNRAS, 334, 847
Leahy, D. A., Yoshida, A., & Matsuoka, M. 1994, ApJ, 434, 341
Matsuoka, M., Kawasaki, K., Ueno, S., et al. 2009, PASJ, 61, 999
McCray, R. A., Shull, J. M., Boynton, P. E., et al. 1982, ApJ, 262, 301
Mihara, T., Makishima, K., & Nagase, F. 1998, AdSpR, 22, 987
Mihara, T., Makishima, K., Ohashi, T., Sakao, T., & Tashiro, M. 1990, Natur, 346, 250
Nagase, F. 2001, in AIP Conf. Ser. 556, Explosive Phenomena in Astrophysical Compact Objects, ed. H.-Y. Chang et al. (Melville, NY: AIP), 56
Neilsen, J., Hickox, R. C., & Vrtilek, S. D. 2004, ApJL, 616, L135
Ng, C., Díaz Trigo, M., Cadolle Bel, M., & Migliari, S. 2010, A&A, 522, A96
Ogilvie, G. I., & Dubus, G. 2001, MNRAS, 320, 485
Parmar, A. N., Pietsch, W., McKechnie, S., et al. 1985, Natur, 313, 119
Pravdo, S. H., Boldt, E. A., Holt, S. S., Rothschild, R. E., & Serlemitsos, P. J. 1978, ApJL, 225, L53
Pringle, J. E. 1996, MNRAS, 281, 357
Ramsay, G., Zane, S., Jimenez-Garate, M. A., den Herder, J.-W., & Hailey, C. J. 2002, MNRAS, 337, 1185

Reynolds, A. P., & Parmar, A. N. 1995, A&A, 297, 747
Reynolds, A. P., Quaintrell, H., Still, M. D., et al. 1997, MNRAS, 288, 43
Romanova, M. M., Ustyugova, G. V., Koldoba, A. V., & Lovelace, R. V. E. 2002, ApJ, 578, 420
Romanova, M. M., Ustyugova, G. V., Koldoba, A. V., & Lovelace, R. V. E. 2004, ApJ, 610, 920
Romanova, M. M., Ustyugova, G. V., Koldoba, A. V., Wick, J. V., & Lovelace, R. V. E. 2003, ApJ, 595, 1009
Scott, D. M., Leahy, D. A., & Wilson, R. B. 2000, ApJ, 539, 392
Shulman, S., Friedman, H., Fritz, G., Henry, R. C., & Yentis, D. J. 1975, ApJL, 199, L101
Staubert, R., Ducci, L., Ji, L., et al. 2020, A&A, 642, A196
Staubert, R., Klochkov, D., Fürst, F., et al. 2017, A&A, 606, L13
Staubert, R., Klochkov, D., Vasco, D., et al. 2013, A&A, 550, A110
Staubert, R., Klochkov, D., Vybornov, V., Wilms, J., & Harrison, F. A. 2016, A&A, 590, A91
Staubert, R., Klochkov, D., & Wilms, J. 2009, A&A, 500, 883
Staubert, R., Shakura, N. I., Postnov, K., et al. 2007, A&A, 465, L25
Stelzer, B., Wilms, J., Staubert, R., Gruber, D., & Rothschild, R. 1999, A&A, 342, 736
Still, M., O'Brien, K., Horne, K., et al. 2001, ApJ, 553, 776
Tananbaum, H., Gursky, H., Kellogg, E. M., et al. 1972, ApJL, 174, L143
Truemper, J., Pietsch, W., Reppin, C., et al. 1978, ApJL, 219, L105
Verner, D. A., Ferland, G. J., Korista, K. T., & Yakovlev, D. G. 1996, ApJ, 465, 487
Vrtilek, S. D., & Cheng, F. H. 1996, ApJ, 465, 915
Vrtilek, S. D., & Halpern, J. P. 1985, ApJ, 296, 606
Wilms, J., Allen, A., & McCray, R. 2000, ApJ, 542, 914
Wojdowski, P., Clark, G. W., Levine, A. M., Woo, J. W., & Zhang, S. N. 1998, ApJ, 502, 253
Zane, S., Ramsay, G., Jimenez-Garate, M. A., den Herder, W. J., & Hailey, C. J. 2004, MNRAS, 350, 506